Soft Fluidic Actuator for Locomotion in Multi-Phase Environments

Roza Gkliva and Maarja Kruusmaa

***Abstract*—This letter presents the design, development, and experimental assessment of a soft fluidic actuator that can enable locomotion in a variety of aquatic and terrestrial environments. Most actuation strategies for amphibious locomotion rely on rigid, fast moving components to generate thrust and tractive forces. Our prototype, comprising soft materials, and relying on simple motion planning and control strategies, demonstrates two gaits, that we employ for locomotion in two vastly different scenarios, underwater swimming and moving on granular terrain with varying levels of water content. By adjusting its internal pressure, the actuator dynamically varies its stiffness and shape, and transitions between wheel and soft paddle form. Experimental results of locomotion in controlled laboratory conditions serve as proof-of-concept for the proposed actuator's efficacy. Using two different motion patterns and control schemes, we show that this prototype achieves both thrust and tractive forces.**

***Index Terms*—Amphibious locomotion, hydraulic/pneumatic actuators, soft robot materials and design.**

I. Introduction

TRADITIONAL methods of terrestrial locomotion include wheels and tracks, with legged configurations gaining in popularity [1]. Aquatic locomotion counterparts include combinations of propellers and lift-based control surfaces or multi-thruster systems [2]. These methods have a proven record of highly efficient and agile locomotion in their respective applications. However, their performance declines significantly when manoeuvering is needed in unstructured, unstable environments, as well as when transitioning through drastically different environments. To mitigate the diminishing performance of locomotion in these conditions, the research community is exploring alternative methods of locomotion, including hybrid designs [3], [4] and compliant materials [4], [5]. In this work, we use these two strategies to develop and study actuation methods for locomotion in aquatic and terrestrial environments, as well as through multi-phase environments such as shore zones (Fig. 1).

Manuscript received 22 March 2022; accepted 13 July 2022. Date of publication 19 July 2022; date of current version 4 August 2022. This letter was recommended for publication by Associate Editor P. Chirarattananon and Editor Y. -L. Park upon evaluation of the reviewers' comments. This work was supported in part by the European Union's Horizon 2020 Research and Innovation Programme ROBOMINERS under Grant Agreement 820971, and in part by the Estonian Research Council under Grant PRG1243 Multiscale Natural Flow Sensing for Coasts and Rivers. *(Corresponding author: Roza Gkliva.)*

The authors are with the Centre for Biorobotics, Department of Computer Systems, Tallinn University of Technology, 12618 Tallinn, Estonia (e-mail: roza.gkliva@ttu.ee; maarja.kruusmaa@ttu.ee).

This letter has supplementary downloadable material available at https://doi.org/10.1109/LRA.2022.3192204, provided by the authors.

Digital Object Identifier 10.1109/LRA.2022.3192204

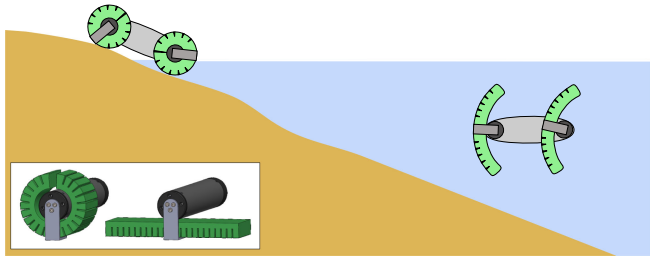

Fig. 1. Illustration of a concept vehicle using the proposed actuator. Top left: the fully pressurized, stiffer actuator generates tractive forces enabling terrestrial locomotion by rotating around a motor shaft. Right: the softer actuator generates propulsive forces enabling underwater swimming by oscillating around the motor shaft. Inset: CAD model of the actuator in both states.

A C-shaped compliant leg design, was used to demonstrate exceptionally agile locomotion, enabling the RHex vehicle to negotiate terrains of varying complexity [6]. This work was instrumental for the development of a series of actuators and robots, aimed at studying amphibious locomotion using appendages that resemble wheels or curved legs and compliant flippers, by manually [7] or dynamically [8]–[10] switching between curved leg or wheel, and flat fin.

Mechanically simpler mechanisms, that employ underactuated and partially passive configurations, have also successfully demonstrated amphibious locomotion. A design combining a circular 1-DOF leg and flat flipper [11], and a similar actuator comprising a stiff fan-shaped leg and a flipper with manually variable stiffness [12] have demonstrated locomotion on terrestrial and aquatic environments. A design comprising a stiff leg with a grate-like morphology, covered by a compliant flap that transforms the leg into a paddle and passively optimizes drag forces during swimming, allowed the RoboTerp quadruped to transition between walking on land and swimming on the water surface [13]. A flat paddle 1-DOF mechanism with a passive elastic hinge enabled underwater walking and swimming for the PEAR hexapod [14].

The strategies mentioned above include rigid, and/or fast moving parts, that can be damaging to the environment or to the robot itself, and can generate large unwanted accelerations in the robot's motion. The combination of rapid impacts of rigid actuators on granular and deformable terrains has additional negative effects on locomotion performance, resulting in reduced traction or the actuators digging into the ground. Integrating compliant parts into locomotion mechanisms can introduce benefits such as increased safety when interacting with the environment, the ability to store and release energy through passive elastic

components, as well as improved quality of motion when negotiating unstructured environments [4]. Completely or partially soft robots have been developed to study amphibious locomotion. A variable stiffness material-pneumatic prototype [15] was used to investigate the dynamic switch between leg and flipper form by adjusting the temperature and internal pressure of its components. Despite its slow actuation, this method shows promising results mostly due to the decoupling of stiffness and shape. A sea urchin-inspired amphibious robot using actuated rigid spines and extensible soft legs was used to investigate bio-inspired locomotion patterns in aquatic and terrestrial conditions [16]. A quadruped robot comprising groups of interconnected thin and soft McKibben actuators demonstrated locomotion on wet and dry terrains, using a variety of walking and crawling gaits [17]. A worm-inspired soft robot, featuring serially connected and individually driven pneumatic actuators, was used to investigate crawling and swimming gaits [18].

In this letter we propose a 1-DOF, reconfigurable, soft fluidic actuator (Fig. 1). Comparing to previous implementations of actuators in similar environments, our prototype employs a rather simple mechanism that allows to dynamically modify its shape and stiffness. Its morphology and compliant material, in combination with simple control and motion planning strategies, enable locomotion in aquatic, terrestrial, and in multi-phase environments. The reconfiguration of the actuator's shape and functionality is achieved by varying its internal pressure. Its locomotion performance was evaluated via a series of experiments in controlled laboratory conditions. To our knowledge, this is the first soft fluidic actuator of this kind to be used for amphibious locomotion. The compliant material and its simplicity of actuation can lead to more widespread usage of this type of actuator, especially in applications where less invasive presence is required.

The contributions of this work include the development of an actuator with the following characteristics:

- **Flexibility of locomotion:** We provide experimental proof-of-concept for locomotion in aquatic, terrestrial and mixed environments.
- **Simplicity of reconfiguration and actuation:** The actuator transitions between its two states by simply varying its internal pressure, enabling a variety of locomotion modes. Actuation relies on 1-DOF rotational or oscillatory motion patterns.
- **Simplicity of design and fabrication:** 3D-printed moulds, wax, and a commercially available composite silicone are the main components used for fabrication.

In what follows we describe the actuator concept, including its design and fabrication (Section II), the experimental evaluation, including test rigs, experimental protocols, as well as motion patterns and controllers that were implemented (Section III). Experimental results and a discussion on the efficacy of the proposed prototype are in Section IV.

II. Actuator Concept and Fabrication

The design of this concept actuator was inspired by the fast PneuNet design described in [19]. PneuNet actuators consist of a soft elastomeric part that contains a network of interconnected air chambers and optionally include flexible strain-limiting elements that affect the actuator's bending profile [20], [21]. Their shape can be controlled by adjusting the internal pressure. Despite their relatively simple design and actuation, their reliability and robustness [19], [22] have made them attractive for a variety of applications. They have been used mainly to study grasping [23], rehabilitation [24], as well as locomotion [22], [25], [26].

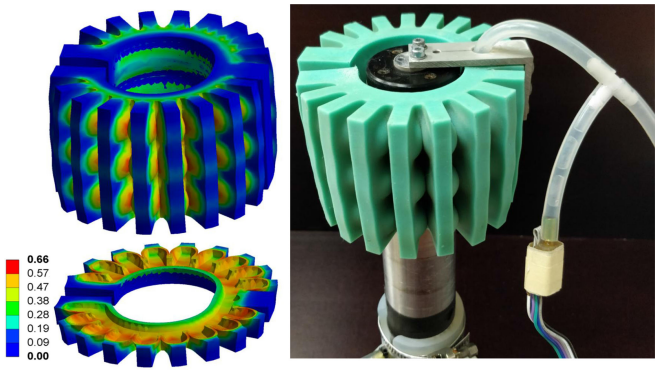

Fig. 2. Deformation due to pressure increase of 100 kPa. Left: equivalent elastic strain levels in a FEM simulation (Ansys), Right: the physical actuator with a fluid intake tube and a pressure sensing module.

We hypothesize that because this design allows the dynamic adjustment of the actuator's stiffness and shape, it is suitable for locomotion in a variety of different conditions, premise partly supported by [12]. By increasing the internal pressure in the actuator, its internal cavities expand. Due to a non-extensible fabric embedded in its flat side, it is constrained from elongation and is deformed as seen in Figs. 1 and 2. With increased internal pressure, in its cylindrical shape, and wrapped around the motor canister, it is stiffer and can better withstand radial and tangential forces. This makes it appropriate to function as a wheel and generate tractive forces by rotating around the motor shaft.

When the internal pressure in the actuator is kept at levels that do not cause deformation, it can be used to generate propulsive forces by performing oscillations around the motor shaft, functioning as a pair of bilateral paddles. Splitting the actuator vertically into two halves, and examining each half separately as an individual paddle, we can look into the actuation cycle's reciprocating motion consisting of two phases: a power phase and a recovery phase. During the recovery phase, the force that is applied to the actuator's external surface, because of the motor's oscillatory motion pattern, causes the paddle to bend towards its smooth side. During the power phase, the segmented geometry on the other side of the actuator prevents bending in the other direction. We hypothesize that this asymmetry will result in a positive net force throughout the actuation cycle, that can be used to generate thrust forces while submerged.

A. FEM Static Analysis

A nonlinear FEM simulation was used to predict the actuator's bending behaviour and to determine the morphology and dimensions appropriate for the experimental validation described

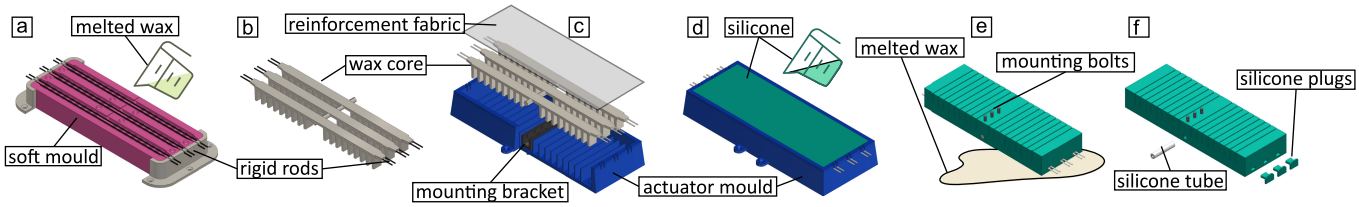

Fig. 3. The fabrication process: (a) metal rods ($\varnothing .5\,\mathrm{mm}$) are suspended over a soft mould on two 3D-printed brackets. These rods provide stability to the wax core, and serve as attachment points during casting the actuator. Melted wax is poured into the mould. (b) After setting, the wax core is demoulded and cleaned of excess wax. (c) An aluminium bracket with a series of bolts attached to it, the wax core and a reinforcement fabric are assembled into the mould. The bolts are used to fasten the cured actuator to a motor shaft. (d) Silicone is mixed, degassed and poured into the mould. (e) After a second degassing and curing, the silicone actuator is demoulded, the wax is melted off at 80°C and pours out from openings on its sides. (f) After the wax and metal rods have been removed and traces of wax have been cleaned, silicone plugs and an intake silicone tube are glued in using Sil-Poxy by Smooth-On.

TABLE I
PROTOTYPE SPECIFICATIONS

Dimensions at rest	$17 \times 6 \times 2\,\mathrm{cm}$
Soft actuator mass	$0.25\,\mathrm{kg}$
Silicone	Elite Double 22 (Zhermack)
Silicone hardness	22 Shore A
Elongation at break	450%
Reinforcement fabric	Art.Nr:09502-003-000007 (KauPo)

TABLE II
SENSORS FOR DATA ACQUISITION

Description	Model	Sampling Rate	Experiment type
Angular position	maxon hall sensors	100 Hz	underwater
Angular velocity	maxon hall sensors	10 Hz	terrestrial
Current	INA219 by TI	100 Hz	both
Force/Torque	ATI Axia80-m20	100 Hz	underwater
Pressure	MS5407-AM	50 Hz	both
Displacement	VL53L0X	40 Hz	terrestrial

in this work. For this analysis we used a hyperelastic model of the actuator's material, the actuator's geometry from a 3D CAD model, and a set of boundary conditions described below. The results included the equivalent elastic stress and strain, and the total deformation.

To characterize the material, we ran tensile tests with specimens made of Elite Double 22 silicone compound by Zhermack (Badia Polesine (RO), Italy). We used an Instron 5866 uniaxial testing machine and followed the ASTM D412 standard [27] for Vulcanized Rubber and Thermoplastic Elastomers. To simulate the actuator's behaviour in Ansys a 3^{rd} order Yeoh model was used, as it can describe deformation under large strains using limited data [28]. Assuming incompressibility of the material, the model takes the form:

$$W(I_1) = \sum_{i=1}^{3} C_{i0}(I_1 - 3)^i. \tag{1}$$

Here, $I_1 = \lambda_1^2 + \lambda_2^2 + \lambda_3^2$ is the first invariant of the three principal stretch ratios, and $C_{10} = 78783\,\mathrm{Pa}$, $C_{20} = 16732\,\mathrm{Pa}$, and $C_{30} = 6618.5\,\mathrm{Pa}$ are the material constants obtained from fitting the tensile experiment data to the 3^{rd} order Yeoh model. For the purpose of the simulations, the density of the material was experimentally estimated as $\rho = 1164\,\mathrm{kg}\,/\,\mathrm{m}^3$.

The model was verified using a scaled-down partial version of the actuator and comparing to simulated results. To determine the simulation boundary conditions, the actuator's internal pressure was measured while it was pressurized until it reached a desired point of deformation after which it was allowed to return to rest. Due to its incompressibility, water was used to increase the internal pressure [19], to apply a consistent pressure on the internal walls of the actuator and on the pressure sensor.

To generate the final design of the actuator, the model was used in an iterative process of design and simulation cycles [29], using SolidWorks to modify the CAD model and Ansys Workbench to run FEM simulations. The following settings and boundary conditions were used in a static structural simulation in Ansys Workbench [29], [30]. a) The external surface surrounding the fixation bolts was defined as a "fixed support". b) All internal surfaces were used to apply pressure, normal to these surfaces. c) The external surfaces between the chambers were defined as "frictionless contact" pairs, to prevent the actuator geometry from penetrating itself. d) The contact between the inextensible layer and the hyperelastic material was defined as a "bonded contact".

The inextensible elastic layer was modelled using a 1^{st} order Yeoh model with material constant $C_{10} = 7.9\,\mathrm{MPa}$ [31]. The aim of this process was to find a geometry that can achieve the desired deformation without failing under load. The number and geometry of chambers, the wall thickness, as well as the gap size between chambers, were modified to achieve the desired bending profile [30]. The inextensible layer thickness and total length of the actuator were constant, and were determined by the thickness of the strain limiting fabric and by the radius of the motor canister respectively. While this design borrows its main features from the original PneuNet actuators, it differs in using a fixation point and fluid intake in the middle of the actuator, as well as using three parallel networks of chambers, compared to the traditional single network configuration. A simulation and the prototype of the final design can be seen in Fig. 2 deformed under $100\,\mathrm{kPa}$ of added pressure.

B. Prototype Fabrication

The fabrication of the actuator follows a two-step lost-wax casting process. During the first step (Fig. 3(a), (b)), a wax core is created, that will be used to create the actuator's internal cavity network. During the second step (Fig. 3(c)–(f)) the wax core is

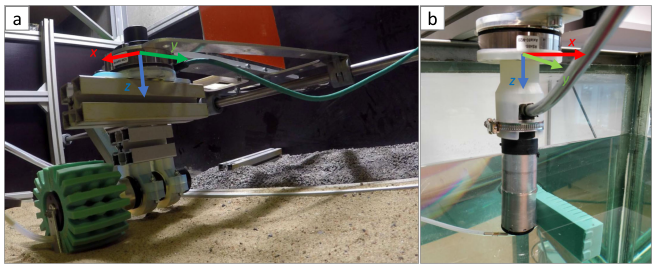

Fig. 4. Experimental testbeds. a: terrestrial, b: underwater.

used in a 3D-printed mould, to cast a soft actuator. The final specifications of the actuator can be seen in Table I.

This method of fabrication may be slightly more challenging compared to the traditionally popular method of casting the top and bottom parts of the actuator separately and then bonding them together [32]. However, in this case, it produces more consistent results, with fewer failure points.

III. Experiments

To validate our hypothesis regarding the suitability of the actuator for locomotion in underwater and terrestrial conditions, we ran experiments separately for these two scenarios, as described in the following subsections. For both scenarios, the soft actuator was mounted on a waterproofed BLDC motor (EC-max 30 by Maxon Motors) driven by an EPOS2 36/2 motor controller, such that it was allowed to fully deform and rotate around the motor shaft (Fig. 4, and accompanying video). Two different combinations from an array of sensors (Table II) were employed in the two test rigs. The data acquisition was performed by a Windows PC running Matlab scripts and a multi-rate Simulink model under Real-Time Desktop in external mode. Sampling rates were chosen to minimize data acquisition latency.

To achieve locomotion in aquatic and terrestrial environments, two motion profiles are required. A continuous rotation of the fully deformed actuator will allow it to generate tractive forces when on ground. An oscillatory motion of the actuator in its low pressure state can generate thrust forces when fully submerged. The motor driver used in these experiments offers a variety of operating modes with different controller structures [33]. For each motion an appropriate control scheme was implemented as described in following sections. All controller gains and feedforward factors were tuned using the "regulation tuning wizard" in the Epos Studio software.

A. Characterization of Blocked Swimming Force

The actuator's efficacy related to generating underwater propulsive forces was evaluated via a series of experiments in a water tank (Fig. 4(b)), focusing on the measurement of forces generated by in-place oscillations.

The oscillatory motion was achieved by prescribing a sinusoidal trajectory with amplitude A and frequency f (Table III) to the motor that the actuator is mounted on. Fig. 5 shows the control scheme employed for the actuator's oscillatory motion. This scheme was implemented in Maxon's EPOS2 Module 36/2

TABLE III
Experiment Parameters

Type of Experiment	Parameter	Range
Underwater	Oscillation amplitude (°) Oscillation frequency (Hz)	$[60, 70, 80, 90]$ $[1.5, 1.75]$
Terrestrial	Angular velocity (rpm) Water content in soil (%)	$[5, 10, 20, 30, 40]$ $[0, 6.25, 12.5, 25]$

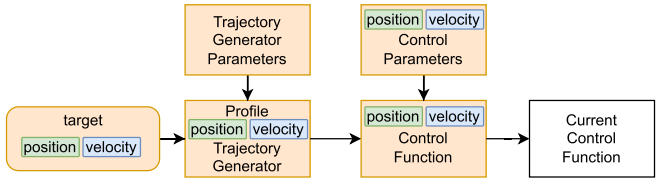

Fig. 5. Control structure for position control (oscillations) and velocity control (rotations). Orange colour denotes scheme-specific functions.

as a position controller using "Profile Position Mode" [34]. This structure employs a position PID controller with a current PI controller as subordinate regulator. At a constant rate, a target position is generated based on the sinusoidal motion profile. The target position is applied to the trajectory generator, which generates a position demand value that is used as input to a position control function. The profile position trajectory generator parameters include the type of motion profile, a velocity profile and an acceleration/deceleration profile that are calculated based on the target position. To protect the motor from high current, velocity and acceleration limits are imposed. The position controller accepts the position demand value and the actual position of the motor shaft. The position control parameters include velocity and acceleration demand values calculated based on the desired A, f, the maximum allowed tracking error, as well as PID controller gains and feedforward factors for velocity and acceleration. The controller output is a current demand value that is fed to the current controller.

For each experiment, the actuator's internal pressure was initially increased by 5–10 kPa, to ensure that the internal chambers maintain their shape, not allowing the actuator to bend backwards. Water was used to increase the internal pressure, to maintain constant buoyancy. Then the actuator was mounted on a force sensor that was suspended over a tank of water, such that the actuator was fully submerged and oriented with its large side normal to the x-axis (Fig. 4(b)). The ranges of A and f were determined empirically, based on position tracking performance, and motion profile limitations described above. The experiment and data acquisition ran for a number of whole periods of actuation, with 10 replicates per A, f combination. The internal pressure of the actuator was measured but not actively controlled.

Post-processing included smoothing of noisy data and calculating evaluation metrics as described bellow. The noise in the current and force data was filtered out using a 10^{th} order Savitzky-Golay filter. A Hampel filter was used to remove outliers in the current measurements. To summarize the results of the experiments, averaged values were calculated using a

number ($n = 7$) of whole actuation periods. To evaluate the controller performance, the amplitude tracking error was calculated by comparing the average actual oscillation amplitude with the nominal desired oscillation amplitude.

$$A_{error} = |A - \left(\bar{\theta}_{high} - \bar{\theta}_{low}\right)| \tag{2}$$

To evaluate the actuator's energetic characteristics, the ratio of propulsive force over the averaged consumed power was used [35], for a number n of whole periods T.

$$\eta = \frac{\overline{F_p}}{\overline{P_{in}}} = \frac{1}{nT}\frac{\int_0^{nT} F_p(t)dt}{\int_0^{nT} VI(t)dt}. \tag{3}$$

Here, $\overline{P_{in}}$ is the averaged consumed power calculated using the measured current consumption $I(t)$ and a constant voltage $V = 24\,\mathrm{V}$, and $F_p(t)$ is the instantaneous propulsive force.

The actuator's first natural frequency has been experimentally estimated using force measurements after manual excitation, and found to be $f_{n,air} = 2.439\,\mathrm{Hz}$ and $f_{n,water} = 1.7241\,\mathrm{Hz}$ while suspended in air and in water respectively.

B. Characterization of Terrestrial Velocity

The actuator's efficacy for locomotion in dry and wet terrestrial conditions was evaluated via a set of experiments on sandy terrain (Fig. 4(a)), focusing on the measurement of the distance travelled by the actuator as it rolls on the ground.

To achieve a wheel-like behaviour and to generate tractive forces, the internal pressure of the actuator is increased until it reaches the desired deformed state, and a constant angular velocity is commanded to its motor. The control scheme used for this purpose (Fig. 5), is implemented as a velocity controller with "Profile Velocity Mode" in Maxon's EPOS2 Module 36/2 [34]. This structure employs a velocity PI controller with a current PI controller as subordinate regulator. A target velocity is sent to the profile velocity trajectory generator, which generates a velocity demand value that is used as input to a velocity control function. The profile velocity trajectory generator parameters include profile acceleration and deceleration values calculated based on a desired acceleration threshold. The velocity controller accepts the velocity demand coming from the trajectory generator as well as the actual angular position of the motor shaft. The velocity control parameters include the velocity controller gains and the feedforward factors for velocity and acceleration. The output is a current demand value that is sent to the current controller along with the current measurement.

Our study includes the transition between aquatic and terrestrial locomotion, such as when a robot would traverse a littoral zone to move from land to water and vice versa. The sand-water-air environment as a three-phase system is appropriate for investigating locomotion in such multi-phase environments, due to the effects of water content to the shear modulus of sand [36]. To address this aspect, the experiment variables included a sweep of actuator angular velocities, as well as varying levels of water content to investigate moving through a multi-phase environment (Table III), with 10 replicates per combination. These parameters were selected based on the hypothesis that they affect the actuator's efficacy and can demonstrate its ability to generate tractive forces in dry and wet conditions, and to examine the multi-phase conditions between the two locomotion scenarios described in this work. The range of the parameters was determined based on visual observations of the water content in the experimental tank, as well as based on limitations of the experimental setup, e.g., limited space for wet sand experiments.

For each experiment, the actuator was mounted on a gantry that slides on a linear guide with reduced friction, allowing motion in 2 DOF: translation along x and rotation around x. Initially, the actuator, mounted on the motor shaft and resting flat on the terrain, was deformed until it achieved "wheel status," by increasing its internal pressure. Then, the motor shaft was actuated to follow a rotational motion pattern, causing the deformed actuator to rotate. The traction forces between the actuator and the soil cause the gantry to move linearly along x. The experiment and data acquisition ended when the gantry had travelled a predetermined distance. The constant pressure to deform the actuator was applied by adding air with a bicycle pump. As pressure did not fluctuate throughout hours of experiments, active control was not necessary.

In post-processing, noisy data was filtered and performance metrics were calculated and summarized as averaged values. The velocity of the gantry along the x-axis was estimated using backwards differentiation of the smoothed (10^{th} order Savitzky-Golay filter) linear displacement.

$$u(t) = \frac{x(t) - x(t-1)}{\tau}, \tag{4}$$

where x is the gantry's position along x at times t and $t-1$, and τ is the time increment.

Assuming no braking during the range of data, the slip ratio of the wheel was calculated based on [37], as:

$$s(t) = \frac{r\omega(t) - u(t)}{r\omega(t)}, \tag{5}$$

where r is the deformed actuator's radius, assuming constant curvature and ω is the angular velocity of the motor shaft.

To evaluate the actuator's energy characteristics, the Cost of Transport metric was used:

$$CoT = \frac{\overline{P_{in}}}{mg\bar{u}} = \frac{1}{nT}\frac{\int_0^{nT} VI(t)dt}{mg\int_0^{nT} u(t)dt}. \tag{6}$$

Here, $m = 2.15\,\mathrm{kg}$ is the mass of the actuator assembly, including the actuator, and all hardware that are moved by it, and excluding the gantry that is balancing on the rail, g is the acceleration of gravity, and $u(t)$ is the gantry's instantaneous velocity along the x direction. Averaged values were calculated over a number n of full periods T or rotation, to account for periodic phenomena in the actuator's motion.

IV. Results and Discussion

The experiments presented here were focused on the evaluation of the actuator's locomotion performance in two drastically different environments, by measuring blocked swimming forces in an aquatic environment and locomotion velocity while traversing sandy terrain. Additionally, we hypothesized that modifying

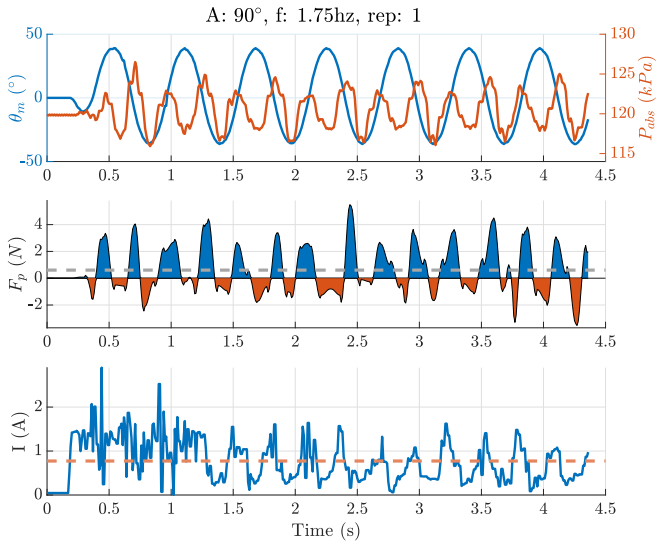

Fig. 6. Indicative underwater force experiment. The upper graph shows the motor's actual position, as it follows a sinusoidal motion pattern, and the internal absolute pressure of the actuator. The middle graph shows the temporal evolution of the instantaneous thrust force. The dashed horizontal line denotes the phase-averaged value, while positive (forward) forces are shaded blue and negative (backward) forces are shaded red. The lower graph shows the instantaneous current consumption of the motor in blue colour and the average current consumption as a dashed horizontal line.

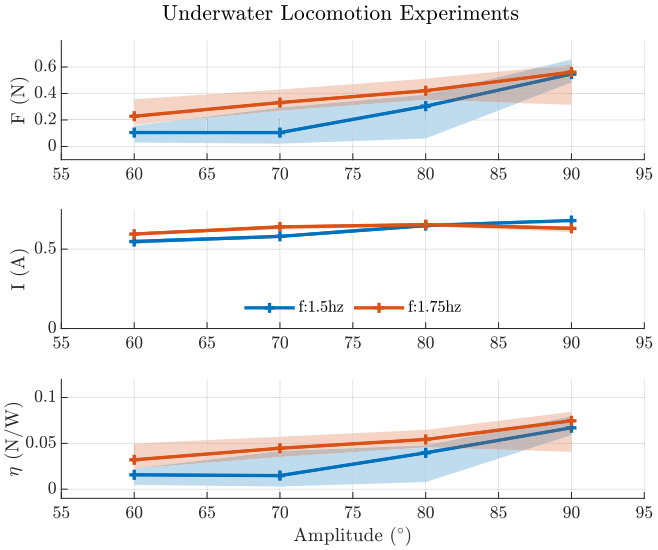

Fig. 7. Aggregate results of underwater experiments. Two frequencies and four amplitudes of oscillation were studied. The crosses show the median values of 10 replicates for each parameter set, with 25^{th} and 75^{th} percentiles as shaded areas. The upper graph shows the evolution of thrust forces, as oscillation amplitude increases, for two frequencies of oscillation. The middle graph shows the median current consumption. The lower graph shows the energetic efficiency metric as described in (3).

the terrain conditions by varying the water content of sand will give us some understanding of the actuator's behaviour in the transition between terrestrial and aquatic locomotion. The following subsections offer a description of the experimental results and a discussion on the two locomotion modes. General discussion on the actuator's performance can be found in Section V.

A. Swimming Forces

Fig. 6 shows indicative underwater experiment results. Examining the pressure measurements in combination with the motor shaft angular position, we observe that the pressure measurement can provide an indication of the actuator's deformation under drag forces that apply pressure to its external surfaces as a result of its own motion in water. This pattern, compared to the pattern of generated thrust forces, shows a correlation between the angular position and velocity of the motor, the internal pressure, and the magnitude and direction of the thrust force. More specifically, while positive force peaks develop during the faster motion of the actuator, when the actuator stops and changes direction of motion, negative forces are generated. During this stop of motion, the elastic behaviour of the material causes the actuator to momentarily return to its original undeformed state, potentially causing these negative forces. This correlation between measured pressure and thrust force could offer a proprioceptive approach for estimating the generated forces. There also seems to be a slight asymmetry in the high and low peaks of the pressure graph, as well as inconsistencies in the duration of the positive and negative forces. These may be attributed to manufacturing inconsistencies, how the actuator is mounted in the test rig, or to waves reflecting off the walls of the test tank and interfering with the measurements.

Fig. 7 offers a summary of the results of the entire sweep of experimental parameters. The upper graph shows that increasing both oscillation parameters generally results in increased thrust forces. The reduced current consumption during faster oscillations ($f = 1.75\,\text{Hz}$) can be attributed to the tested frequency being close to the actuator's first natural frequency. However, while higher frequency shows a higher thrust force trend in the lower amplitudes, the two datasets converge at higher amplitudes, due to increased amplitude tracking error at the ($90°$, $1.75\,\text{Hz}$) parameter set, caused by velocity and acceleration limits set to the motion controller.

The efficiency metric η, shows that this actuator performs worse than previous prototypes designed exclusively for aquatic locomotion [38], [39], mainly due to reduced force generation. While further optimization of the actuator's morphology, motion planning and control can improve this metric, we recognize that the reduced performance is a trade-off that enables locomotion in terrestrial conditions.

B. Terrestrial Velocity

Fig. 8 presents indicative terrestrial experiment results. It is evident that a constant angular velocity of the motor generates a somewhat constant linear velocity of the gantry. A jump that occurs when the actuator is rolling over its seam (e.g., at $5\,\text{sec}$ on Fig. 8) can be corrected with higher internal pressure or with optimizing the actuator dimensions.

Fig. 9 presents a summary of the terrestrial locomotion experiments. These graphs show that increasing the motor's angular

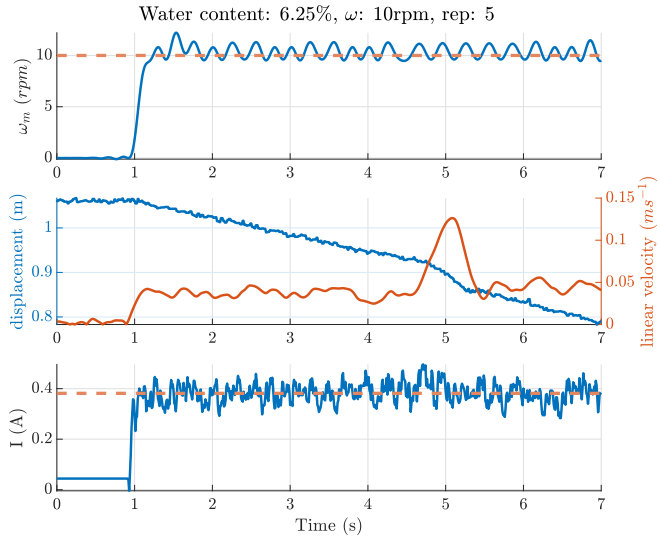

Fig. 8. Indicative terrestrial locomotion experiment in sand. The upper graph shows the actual angular velocity of the actuator's motor shaft. The dashed horizontal line denotes the desired angular velocity. The middle graph shows the temporal evolution of the gantry's position along the rail as it moves towards the distance sensor, as well as the gantry's velocity calculated based on (4). The lower graph shows the instantaneous current consumption in blue colour and the averaged as a red dashed line.

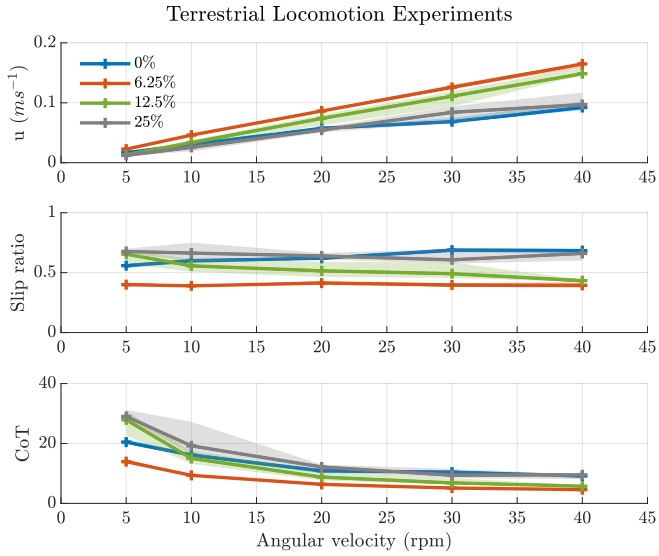

Fig. 9. Aggregate results for terrestrial locomotion experiments. The crosses show the median values of 10 replicates for each parameter set, with 25^{th} and 75^{th} percentiles as shaded areas. The upper graph shows the linear velocity of the gantry for all angular velocities and all levels of water content in the soil. The middle and bottom graphs show the slip ratio and the Cost of Transport calculated based on (5) and (6) respectively.

velocity results in higher linear velocity of the gantry. The gantry velocity is also dependent on the water content level, with the two edge cases (0% and 25%) achieving lower speeds with a nonlinear relationship and the two middle sets (6.25% and 12.5%) achieving consistently higher speeds following a rather linear relationship. This dependence on water content appears also in the middle and bottom graphs, with the two edge sets having a higher slip ratio and Cost of Transport, and the 6.25% set consistently lowest. This behaviour is supported by Fall *et al.* in [36] that showed that some water in sand increases its shear modulus, but too much water decreases it back to levels of dry sand. As a qualitative confirmation of this, we observed visually (see accompanying video) that in loose soil, either dry sand or very wet sand, the actuator can more easily dig itself into the soil if it finds resistance along its direction of motion.

V. Conclusion

We have presented the design and development of a soft fluidic actuator that can enable aquatic and terrestrial locomotion, from fully submerged swimming to negotiating wet and dry granular terrain. This wide range of locomotion is achieved by using a design and a compliant material that allow the actuator to transition between two shapes: paddle and wheel, by modifying the actuator's internal pressure.

Our hypothesis regarding the proposed actuator's locomotion performance was evaluated via a series of experiments in the two target environmental conditions. We also investigated conditions that resemble the transition between aquatic and terrestrial locomotion, by gradually increasing the water content of the soil. The experiments and data analysis justify the actuator design and choice of material, and serve as proof-of-concept. While the performance in either locomotion scenario is suboptimal, we accept this trade-off, as the same design choices allow the easy reconfigurability of shape and stiffness that enables amphibious locomotion. Regarding locomotion on deformable and granular terrains, compared to most stiff-legged amphibious prototypes, this actuator demonstrates relatively low impact motion and does not disturb the terrain as much. This can be very beneficial to a robot's locomotion characteristics, when e.g., exploring areas with fragile ecosystems where low environmental impact is necessary, or when performing data collection where high accelerations can affect data quality.

We hypothesize that a third mode of locomotion, surface swimming, can be achieved by this actuator, using a combination of the two modes described in this letter, i.e., rotating around the motor shaft with low internal pressure, while on the water surface. This mode of locomotion demonstrated in previous literature [40] was not experimentally investigated in this work, but will be part of our future work.

More importantly, we aim to further investigate the transition between locomotion modes, extending the experimental setups to allow more degrees of freedom, including unconstrained underwater and terrestrial locomotion. This will allow investigation of dynamic transitions between modes, such as underwater to surface swimming, surface swimming to terrestrial locomotion, etc. Currently, the transition between the actuator's two forms is achieved by either manually increasing the volume of its internal fluid, or using a bulky pump system. To increase portability and autonomy of the actuator, a mechanism will be developed that will allow the controlled transition between the two forms. Additionally, optimization of motor kinematics and motion planning will be investigated to improve performance.

ACKNOWLEDGMENT

The authors thank Asko Ristolainen for his contributions on the actuator fabrication, as well as Jaan Rebane and Andres Ernits for their support with the experimental setup.

REFERENCES

[1] B. Siciliano and O. Khatib, *Springer Handbook of Robotics*. Berlin, Germany: Springer, 2008.
[2] G. Antonelli, *Underwater Robots*, vol. 3, Berlin, Germany: Springer, 2014.
[3] L. Bruzzone and G. Quaglia, "Locomotion systems for ground mobile robots in unstructured environments," *Mech. Sci.*, vol. 3, no. 2, pp. 49–62, 2012.
[4] M. Calisti, G. Picardi, and C. Laschi, "Fundamentals of soft robot locomotion," *J. Roy. Soc. Interface*, vol. 14, no. 130, 2017, Art. no. 20170101.
[5] D. Rus and M. T. Tolley, "Design, fabrication and control of soft robots," *Nature*, vol. 521, no. 7553, pp. 467–475, 2015.
[6] U. Saranli, M. Buehler, and D. E. Koditschek, "RHex: A simple and highly mobile hexapod robot," *Int. J. Robot. Res.*, vol. 20, no. 7, pp. 616–631, 2001.
[7] C. Georgiades et al., "AQUA: An aquatic walking robot," in *Proc. IEEE/RSJ Int. Conf. Intell. Robots Syst.*, 2004, pp. 3525–3531.
[8] X. Liang et al., "The AmphiHex: A novel amphibious robot with transformable leg-flipper composite propulsion mechanism," in *Proc. IEEE/RSJ Int. Conf. Intell. Robots Syst.*, 2012, pp. 3667–3672.
[9] L. Bai, G. Dou, W. Duan, Y. Sun, J. Zheng, and X. Chen, "Amphibious robot with a novel composite propulsion mechanism," in *Proc. 6th IEEE Int. Conf. Adv. Robot. Mechatron.*, 2021, pp. 442–447.
[10] Y. Sun, S. Ma, and X. Luo, "Design of an eccentric paddle locomotion mechanism for amphibious robots," in *Proc. IEEE Int. Conf. Robot. Biomimetics*, 2010, pp. 1098–1103.
[11] B. B. Dey, S. Manjanna, and G. Dudek, "Ninja legs: Amphibious one degree of freedom robotic legs," in *Proc. IEEE/RSJ Int. Conf. Intell. Robots Syst.*, 2013, pp. 5622–5628.
[12] B. Zhong, S. Zhang, M. Xu, Y. Zhou, T. Fang, and W. Li, "On a CPG-based hexapod robot: AmphiHex-II with variable stiffness legs," *IEEE/ASME Trans. Mechatron.*, vol. 23, no. 2, pp. 542–551, Apr. 2018.
[13] A. R. Vogel, K. N. Kaipa, G. M. Krummel, H. A. Bruck, and S. K. Gupta, "Design of a compliance assisted quadrupedal amphibious robot," in *Proc. IEEE Int. Conf. Robot. Automat.*, 2014, pp. 2378–2383.
[14] T. Kim, Y.-W. Song, S. Song, and S.-C. Yu, "Underwater walking mechanism of underwater amphibious robot using hinged multi-modal paddle," *Int. J. Control, Automat. Syst.*, vol. 19, no. 4, pp. 1691–1702, 2021.
[15] R. L. Baines, J. W. Booth, F. E. Fish, and R. Kramer-Bottiglio, "Toward a bio-inspired variable-stiffness morphing limb for amphibious robot locomotion," in *Proc. 2nd IEEE Int. Conf. Soft Robot.*, 2019, pp. 704–710.
[16] T. Paschal, M. A. Bell, J. Sperry, S. Sieniewicz, R. J. Wood, and J. C. Weaver, "Design, fabrication, and characterization of an untethered amphibious sea urchin-inspired robot," *IEEE Robot. Automat. Lett.*, vol. 4, no. 4, pp. 3348–3354, Oct. 2019.
[17] A. A. M. Faudzi, M. R. M. Razif, G. Endo, H. Nabae, and K. Suzumori, "Soft-amphibious robot using thin and soft McKibben actuator," in *Proc. IEEE Int. Conf. Adv. Intell. Mechatron.*, 2017, pp. 981–986.
[18] E. Milana et al., "EELWORM: A bioinspired multimodal amphibious soft robot," in *Proc. 3rd IEEE Int. Conf. Soft Robot.*, 2020, pp. 766–771.
[19] B. Mosadegh et al., "Pneumatic networks for soft robotics that actuate rapidly," *Adv. Funct. Mater.*, vol. 24, no. 15, pp. 2163–2170, 2014.
[20] F. Ilievski, A. D. Mazzeo, R. F. Shepherd, X. Chen, and G. M. Whitesides, "Soft robotics for chemists," *Angewandte Chemie*, vol. 123, no. 8, pp. 1930–1935, 2011.
[21] B. Gorissen, D. Reynaerts, S. Konishi, K. Yoshida, J.-W. Kim, and M. De Volder, "Elastic inflatable actuators for soft robotic applications," *Adv. Mater.*, vol. 29, no. 43, 2017, Art. no. 1604977.
[22] M. T. Tolley et al., "A resilient, untethered soft robot," *Soft Robot.*, vol. 1, pp. 213–223, 2014.
[23] J. Shintake, V. Cacucciolo, D. Floreano, and H. Shea, "Soft robotic grippers," *Adv. Mater.*, vol. 30, no. 29, 2018, Art. no. 1707035.
[24] P. Polygerinos et al., "Towards a soft pneumatic glove for hand rehabilitation," in *Proc. IEEE/RSJ Int. Conf. Intell. Robots Syst.*, 2013, pp. 1512–1517.
[25] J. Ning, C. Ti, and Y. Liu, "Inchworm inspired pneumatic soft robot based on friction hysteresis," *J. Robot. Automat.*, vol. 1, no. 1, pp. 54–63, 2017.
[26] R. F. Shepherd et al., "Multigait soft robot," *Proc. Nat. Acad. Sci. USA*, vol. 108, no. 51, pp. 20400–20403, 2011.
[27] *Standard Test Methods for Vulcanized Rubber and Thermoplastic Elastomers-Tension*, ASTM D412-16(2021), ASTM International, West Conshohocken, PA, USA, 2021. [Online]. Available: www.astm.org
[28] C. Renaud, J.-M. Cros, Z.-Q. Feng, and B. Yang, "The yeoh model applied to the modeling of large deformation contact/impact problems," *Int. J. Impact Eng.*, vol. 36, no. 5, pp. 659–666, 2009.
[29] C. Tawk and G. Alici, "Finite element modeling in the design process of 3D printed pneumatic soft actuators and sensors," *Robotics*, vol. 9, no. 3, 2020, Art. no. 52.
[30] M. S. Xavier, A. J. Fleming, and Y. K. Yong, "Finite element modeling of soft fluidic actuators: Overview and recent developments," *Adv. Intell. Syst.*, vol. 3, no. 2, 2021, Art. no. 2000187.
[31] P. Polygerinos et al., "Modeling of soft fiber-reinforced bending actuators," *IEEE Trans. Robot.*, vol. 31, no. 3, pp. 778–789, Jun. 2015.
[32] P. Polygerinos et al., "Soft robotics: Review of fluid-driven intrinsically soft devices; manufacturing, sensing, control, and applications in human-robot interaction," *Adv. Eng. Mater.*, vol. 19, no. 12, 2017, Art. no. 1700016.
[33] EPOS2 positioning controllers application notes, maxon motor AG, Sachseln, Switzerland, 2016. [Online]. Available: www.maxongroup.com
[34] EPOS2 positioning controllers firmware specification, maxon motor AG, Sachseln, Switzerland, 2017. [Online]. Available: www.maxongroup.com
[35] J. S. Palmisano, R. Ramamurti, J. D. Geder, M. Pruessner, W. C. Sandberg, and B. Ratna, "How to maximize pectoral fin efficiency by control of flapping frequency and amplitude," in *Proc. 18th Int. Symp. Unmanned Untethered Submersible Technol.*, 2013, pp. 124–132.
[36] A. Fall et al., "Sliding friction on wet and dry sand," *Phys. Rev. Lett.*, vol. 112, no. 17, 2014, Art. no. 175502.
[37] K. Yoshida and H. Hamano, "Motion dynamics and control of a planetary rover with slip-based traction model," in *Proc. Int. Soc. Opt. Photon. Unmanned Ground Veh. Technol.*, 2002, pp. 275–286.
[38] R. Gkliva, M. Sfakiotakis, and M. Kruusmaa, "Development and experimental assessment of a flexible robot fin," in *Proc. IEEE Int. Conf. Soft Robot.*, 2018, pp. 208–213.
[39] A. Simha, R. Gkliva, Ü. Kotta, and M. Kruusmaa, "A flapped paddle-fin for improving underwater propulsive efficiency of oscillatory actuation," *IEEE Robot. Automat. Lett.*, vol. 5, no. 2, pp. 3176–3181, Apr. 2020.
[40] G. Dudek et al., "A visually guided swimming robot," in *Proc. IEEE/RSJ Int. Conf. Intell. Robots Syst.*, 2005, pp. 3604–3609.